

Oxygen Evolution Reaction on Tin Oxides Supported Iridium Catalysts: Do We Need Dopants?

Gabriel C. da Silva,^{*[a, b, c]} Seiti I. Venturini,^[b] Siyuan Zhang,^[d] Mario Löffler,^[a, e] Christina Scheu,^[d] Karl J. J. Mayrhofer,^[a, e] Edson A. Ticianelli,^[b] and Serhiy Cherevko^{*[a]}

Application of oxide supports is considered as a viable approach to decrease iridium loading in oxygen evolution reaction catalysis in acid electrolyte. While the most of the promising oxides are poor conductors, the need for doping is typically taken as granted, and a representative example is tin dioxide. There are still, however, serious concerns on the feasibility of this approach as we lack consensus on any activity gain by using such oxides, while doubts on stability are numerous. In this work, a set of catalyst/support combinations including two catalysts, viz. hydrous (IrO_x) and rutile (IrO₂) iridium oxides, and four supports, viz. SnO₂ and Sb- (ATO), F- (FTO), and In-doped (ITO) SnO₂, are synthesized and character-

ized by a selection of complementary experimental techniques including rotating disk electrode and on-line inductively coupled plasma mass spectrometry. It is found that the electrochemical activity in acid media of supported Ir catalysts is essentially the same, independent on presence or absence of dopants. Sb and In dopants are shown to be unstable and cause an increased dissolution of Sn. Besides, the degradation of the doped supports results in destabilization of iridium oxides. These results raise doubts on the real need for the use of dopants in SnO₂-based catalyst supports for electrochemical water splitting.

1. Introduction

The electrochemical splitting of water into hydrogen, hydrogen evolution reaction (HER) and oxygen, oxygen evolution reaction (OER), by means of water electrolysis is often pointed out as a viable solution to store the energy provided by intermittent renewable sources.^[1] Due to its very slow kinetics, which is typically attributed to the complex four electron reaction mechanism, the OER persists as a major bottleneck in this technology.^[2] In proton exchange membrane water electrolyzers (PEMWEs), Ir-based materials, in particular iridium oxide, are the state-of-the-art OER electrocatalysts due to the combi-

nation of their activity and stability.^[3] However, due to the scarcity and high cost of iridium, its use in PEMWE must be optimized. In this context, the use of catalyst supports have been suggested, since they can enhance the dispersion of the catalyst active phase, resulting in a higher electrochemically active area, allowing the reduction of the noble metal loading and thus of the cost of the PEMWE electrode.^[3–4]

Carbon materials are the most widely used supports in electrocatalysis, because they combine the large surface area, high electrical conductivity, and adequate stability required, for example, in fuel cell applications.^[5] In the anode of PEMWE, however, the high potential in which the OER takes place may cause the oxidation of the carbon to CO₂, making it unfeasible as a catalyst support. To overcome this obstacle, the use of several electrically conductive oxides has been proposed. In this context, SnO₂ is frequently mentioned as a stable and suitable support, despite its lower electrical conductivity compared to carbon.^[6]

In order to achieve higher electrical conductivity, doping of SnO₂ with antimony (ATO), fluorine (FTO), and indium (ITO) atoms has been shown to be a successful strategy,^[7] while satisfactory OER activities were obtained for doped-SnO₂ supported iridium-based catalysts.^[8] However, the stability of these doped supports and, consequently, the stability of the doped-SnO₂ iridium oxide catalysts, is still to be clarified.

In a previous work, our group investigated the dissolution stability of model ATO, FTO and ITO films under high cathodic and anodic potentials.^[9] For ATO and ITO materials, besides the dissolution of Sb and In, a destabilization of Sn was observed, leading to higher dissolution rates compared to that of FTO. Nonetheless, a comparison with pure SnO₂ was not performed, which raises the question: Do we need dopants? Besides, the time- and potential-resolved dissolution stability of doped-SnO₂


[a] Dr. G. C. da Silva, M. Löffler, Prof. K. J. J. Mayrhofer, Dr. S. Cherevko
Helmholtz-Institute Erlangen-Nürnberg for Renewable Energy (IEK-11)
Forschungszentrum Jülich GmbH
Egerlandstr. 3, 91058, Erlangen, Germany
E-mail: gabrieldasilva@iqsc.usp.br
s.cherevko@fz-juelich.de

[b] Dr. G. C. da Silva, S. I. Venturini, Prof. E. A. Ticianelli
São Carlos Institute of Chemistry
University of São Paulo
Av. Trabalhador São-carlense 400, 13560-970,
São Carlos, Brazil

[c] Dr. G. C. da Silva
Federal Institute of Southeastern of Minas Gerais
Rua Monsenhor José Augusto 204, 36205-018,
Barbacena, Brazil

[d] Dr. S. Zhang, Prof. C. Scheu
Independent Research Group Nanoanalytics and Interfaces
Max-Planck-Institut für Eisenforschung GmbH
40237 Düsseldorf, Germany

[e] M. Löffler, Prof. K. J. J. Mayrhofer
Department of Chemical and Biological Engineering
Friedrich-Alexander-Universität Erlangen-Nürnberg
Egerlandstr. 3, 91058 Erlangen, Germany

 Supporting information for this article is available on the WWW under
<https://doi.org/10.1002/celec.202000391>

supported iridium oxide catalysts, to the best of our knowledge, have not been accessed so far.

Herein, hydrous (IrO_x) and rutile (IrO_2) iridium oxide nanoparticles were deposited on SnO_2 , ATO, FTO, and ITO supports. The synthesized catalysts were characterized using several physicochemical techniques, and their electrochemical activity and stability were investigated in acid media, combining a conventional rotating disk electrode (RDE) setup and a scanning flow cell hyphenated to an inductively coupled plasma mass spectrometer (SFC-ICP-MS). The catalysts' activities for the OER and dissolution data are used to evaluate the feasibility of undoped and doped- SnO_2 as catalyst supports in acidic media.

Experimental Section

Synthesis of the Electrocatalysts

Synthesis of the SnO_2 and doped SnO_2 supports

The tin oxide support was prepared as described by Oh et al.^[7] Briefly, 1.28 g of dodecylamine (98%, Sigma-Aldrich) was added to an ethanol solution (65 mL of ethanol + 160 mL of deionized water), with constant stirring for 3 h. A solution consisting of 20 mL of ethanol and 5.21 g of tin(IV) chloride (99.99%, Alfa Aesar) was added to the dodecylamine suspension, and stirred for 1 h. The resulting suspension was refluxed for 72 h at 80 °C, and cooled down to room temperature. A white precipitate was obtained with centrifugation at 5000 rpm for 10 min, which was then washed with deionized water. The solid powder was dispersed in 20 mL of deionized water and transferred to a polytetrafluorethylene (PTFE) chamber in a stainless steel autoclave reactor, and heated at 120 °C for 24 h. The obtained oxide was filtered and washed with ethanol, and then calcined at 400 °C for 3 h in air atmosphere.

Antimony-doped tin oxide (ATO), fluorine-doped tin oxide (FTO), and indium-doped tin oxide (ITO), were obtained using different compositions of the metal precursor solution. ATO was obtained using a solution consisting of 20 mL of ethanol, 4.79 g of tin(IV) chloride (99.99%, Alfa Aesar) and 0.48 g of antimony(III) acetate (97%, Alfa Aesar). FTO was obtained using a solution consisting of 30 mL of ethanol, 2.61 g of tin(IV) chloride (99.99%, Alfa Aesar) and 0.38 g of ammonium fluoride hydrate (99.9975%, Alfa Aesar). ITO was obtained using a solution consisting of 60 mL of ethanol, 2.11 g of tin(IV) chloride (99.99%, Alfa Aesar) and 0.15 g of indium (III) chloride (98%, Alfa Aesar).

Synthesis of supported IrO_x catalysts

Hydrous iridium oxide (IrO_x) was deposited on the different SnO_2 -based supports to a nominal Ir loading of 20 wt% using a hydrothermal method.^[10] Initially, a solution of the iridium precursor was prepared by dissolving 5 g of $\text{H}_2\text{IrCl}_6 \cdot x\text{H}_2\text{O}$ (99%, Alfa Aesar) in 100 mL of deionized water. A given amount of 1 M solution of LiOH (99%, Sigma-Aldrich) was added to 1 mL of the iridium precursor solution, under stirring, so to reach a final ratio of $[\text{OH}^-]/[\text{Cl}^-] = 6$. A mass of 96 mg of the SnO_2 -based support was then added to the iridium solution, the volume was raised to 50 mL with the addition of ultrapure water, and the resulting suspension was kept under stirring for 3 h. The mixture was transferred to a PTFE chamber in a stainless steel autoclave reactor, and heated at 180 °C for 24 h. The supported catalyst was filtered, washed with water, and dried at 50 °C for 1 h.

Synthesis of supported IrO_2 catalysts

Rutile iridium oxide (IrO_2) supported on the SnO_2 -based materials was obtained by calcination of the supported hydrous (IrO_x) samples at 600 °C for 3 h in air.

Physicochemical characterization

Energy dispersive X-ray spectroscopy (EDX) analyses of the synthesized electrocatalysts was performed in a Leica-Zeiss LEO 440 scanning electron microscope operating at 40 kV. The catalysts' crystalline structure was investigated by X-ray diffraction in a Bruker D8 Advance diffractometer with $\text{Cu-K}\alpha$ radiation (1.5406 Å); the data were collected for 2θ values between 10 and 100° at a rate of $0.075^\circ \text{s}^{-1}$. The structural parameters of the catalysts were calculated using the Rietveld refinement method.^[11]

Transmission electron microscopy (TEM) images were obtained in a JEOL JEM2100 microscope operated at 200 kV. The scanning transmission electron microscopy (STEM) and EDX chemical mapping were performed on a Titan Themis microscope operated at 300 kV. Atomic number contrast STEM micrographs were recorded by the high angle annular dark field (HAADF) detector with collection half-angles between 73 and 200 mrad. EDX spectrum imaging was collected using the SuperX system with four silicon drift detectors. Multivariate analysis of the spectrum imaging datacubes was conducted to reduce the noise and identify the spatial distribution of related X-ray peaks.^[12]

X-ray photoelectron spectroscopy (XPS) analyses was carried out in a Quantera II instrument, with monochromatic Al $\text{K}\alpha$ X-rays (1486.6 eV), operating under ultrahigh vacuum conditions. All XPS spectra were calibrated according to the C 1s peak energy at 284.8 eV.

The electrical conductivity of the synthesized materials was measured by compressing the catalyst powders into 1 mm thick pellets between two steel pistons in a glass tube (3.0 mm inner diameter) under a pressure of 25 MPa. Current between the two probes was supplied by a HP 6033 A power supply, while potential was recorded with a voltmeter. Electrical conductivity values were calculated using Ohm's law.

Electrochemical Measurements

Electrochemical characterization and OER activities

The electrochemical measurements were performed in a three-electrode electrochemical cell, in argon-purged 0.1 M H_2SO_4 electrolyte at 25 °C. A reversible hydrogen electrode (RHE) and a graphite rod were used as reference and counter electrodes, respectively. A catalyst ink was prepared by dispersing 4 mg of the catalyst powder and 15 μL of Nafion (5 wt%, Alfa Aesar) in 1 mL of ultrapure water (18.2 M Ω cm, Milli-Q). The working electrode was prepared by depositing the ink on a glassy carbon electrode (area of 0.196 cm²) to a final Ir loading of 75 $\mu\text{g cm}^{-2}$.

The synthesized materials were initially characterized by cyclic voltammetry (CV) experiments recorded between 0.05–1.2 V at 50 mV s⁻¹. The catalysts' activities for the OER were evaluated with linear sweep voltammeteries (LSVs) between 1.1–1.6 V at 5 mV s⁻¹, while the working electrode was kept at a rotation of 1600 rpm. Ohmic drop correction was performed by the determination of the high-frequency resistance in a typical electrochemical impedance spectroscopy (EIS) experiment from 100 kHz to 0.1 Hz with a voltage perturbation of 10 mV under open-circuit potential (not shown).

Accelerated stability test

The catalysts' stability was evaluated using an accelerated stability test (AST) which consisted of 1,000 potential cycles between 1.1–1.6 V at 400 mV s⁻¹. The catalytic performance of the synthesized materials was evaluated before and after the degradation protocol by LSVs between 1.1–1.6 V at 5 mV s⁻¹. The working electrode was kept under a rotation of 1600 rpm during AST.

Electrochemical dissolution of catalysts

Electrochemical dissolution experiments were conducted in a scanning flow cell hyphenated to an inductively coupled plasma mass spectrometer (Perkin Elmer NexION 300X), as described elsewhere.^[9,13] Argon-purged 0.1 M H₂SO₄ solution, at 25 °C, with a flow of 175 μL min⁻¹ was used as the electrolyte, while an Ag/AgCl electrode (3 M) and a graphite rod were employed as reference and counter electrodes, respectively. The measured potentials were converted to the RHE scale according to the Nernst equation: $E_{\text{RHE}} = E_{\text{Ag/AgCl}} + E^0_{\text{Ag/AgCl}} + 0.059 \text{ pH}$. The working electrodes consisted of small catalyst spots (diameter of ~0.8 mm) obtained by drop casting the catalyst ink on a glassy carbon plate, resulting in a final Ir loading of 0.5 μg/spot (ca. 25 μg cm⁻²).

Daily calibration of the ICP–MS was done using Ir, Sn, Sb, and In standard solutions with concentration of 0.5, 1, and 5 ppb, whereas a steady performance was ensured using internal standard solutions (¹⁸⁷Re, ¹⁰³Rh, ¹³⁰Te).

Three protocols were used to evaluate the catalysts' dissolution: i) three potential cycles between 1.1–1.6 V, at 5 mV s⁻¹; ii) a ramp to a final 5 mA cm⁻² current density, at 5 mV s⁻¹; iii) 1,000 potential cycles between 1.1–1.6 V at 400 mV s⁻¹, which is analogous to the AST used in the RDE setup. Before each protocol, 10 cleaning potential cycles between 0.05–1.2 V at 200 mV s⁻¹ were performed.

2. Results

2.1. Characterization of Catalysts

The EDX mass compositions of the synthesized electrocatalysts are shown in Tables S1 and S2. Regarding the hydrous IrO_x catalysts (Table S1), the iridium contents in the different materials are close to the nominal value of 20 wt%, while the concentrations of antimony, fluorine and indium correspond to 6%, 2% and 4% of the mass composition of the ATO-, FTO-, and ITO-supported catalysts, respectively. After the heat treatment at 600 °C for 3 h, one can see that the compositions of rutile IrO₂ materials (Table S2) are close to those obtained for the hydrous samples within the experimental error, evidencing no significant deviations from the expected amounts of iridium or dopants.

The X-ray diffractograms of the IrO_x/SnO₂ and IrO₂/SnO₂ catalysts are shown in Figure 1. The XRD pattern of the IrO_x/SnO₂ catalyst exhibits peaks corresponding to the cassiterite tetragonal SnO₂ structure (vertical red lines, PDF 3-439).^[14] Similar profiles are seen for the materials with the doped SnO₂ supports (Figure S1a). For the IrO₂/SnO₂ annealed catalyst, one can note the existence of thin peaks as shoulders of the peaks corresponding to the SnO₂ phase. These peaks can be attributed to the tetragonal IrO₂-rutile structure (vertical gray

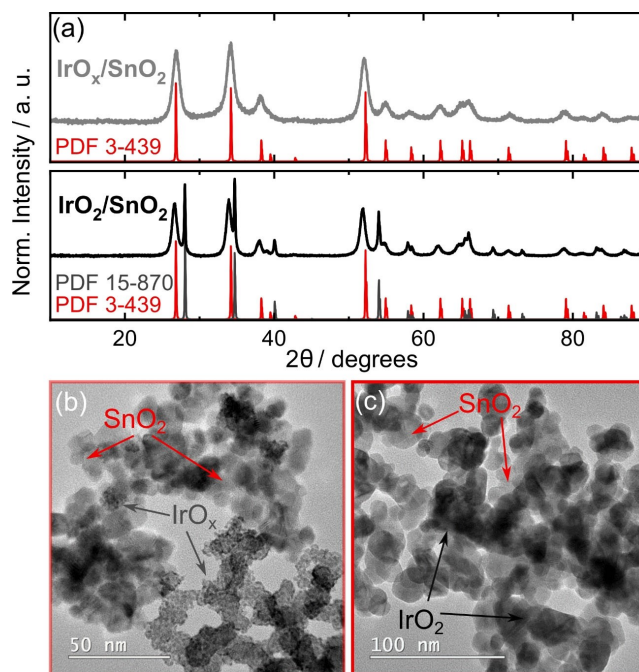


Figure 1. a) Normalized X-ray diffractograms of the IrO_x/SnO₂ and IrO₂/SnO₂ catalysts. Red and gray vertical lines correspond to the SnO₂ (PDF 3-439) and IrO₂ (PDF 15-870) structures, respectively. Transmission electron micrographs of the b) IrO_x/SnO₂ and c) IrO₂/SnO₂ catalysts.

lines, PDF 15-870),^[15] and are also observed for the IrO₂/ATO, IrO₂/FTO, and IrO₂/ITO materials (Figure S1b), confirming that the amorphous IrO_x phase in the catalyst was converted to the crystalline IrO₂.

The structural parameters calculated for the different materials are exhibited in Table S3. The mean crystallite size (*D*) of the SnO₂ phase in the IrO_x/SnO₂ (6.2 nm) is larger than those calculated for the samples containing the doped supports, which are approximately 3.5 nm. Due to its amorphous nature, the structural parameters of the IrO_x phase in the catalysts could not be calculated. After the calcination procedure, the mean crystallite size of the SnO₂ particles increases to 8 nm in the IrO₂/SnO₂ catalyst and to ~5 nm for IrO₂/ATO, IrO₂/FTO, and IrO₂/ITO materials. With respect to the IrO₂ particles, the mean crystallite sizes calculated for the SnO₂-, ATO-, FTO-, ITO-supported catalysts are 22.2, 28.9, 30.9 and 16.1 nm, respectively, which are larger than that calculated for the unsupported IrO₂ (12.9 nm) catalyst synthesized by the same method.

TEM micrographs of the IrO_x/SnO₂ and IrO₂/SnO₂ catalysts are shown in Figure 1b,c. For the IrO_x/SnO₂ material (Figure 1b), small IrO_x nanoparticles ranging between 1–2 nm deposited and anchored on bigger SnO₂ particles of support are observed. The unsupported IrO_x catalyst consists of particles of similar sizes as shown in Figure S2. Also, the doped supports have morphology similar to those of the IrO_x/SnO₂ catalyst (Figure S3). All supported catalysts exhibit regions with circular agglomerates of IrO_x nanoparticles as shown in Figures S3b and S3c for IrO_x/FTO and IrO_x/ITO. A higher magnification image and an EDX chemical mapping of two of these agglomerates are shown in Figures S4 and S5, respectively. We attribute the

presence of such agglomerates to peculiarities of the chosen synthesis procedure.

Regarding the $\text{IrO}_2/\text{SnO}_2$ catalyst (Figure 1c), the existence of higher contrast particles supported on a lower contrast phase is observed, as indicated in the micrograph, corresponding to IrO_2 and SnO_2 nanoparticles, respectively. The micrographs obtained for the IrO_2/ATO , IrO_2/FTO , and IrO_2/ITO materials are shown in Figure S6, in which the presence of particles with sizes ranging between 20–30 nm can be seen, and this is in agreement with the XRD results for the IrO_2 mean crystallite size in these catalysts (Table S3). The TEM image of the unsupported IrO_2 catalyst can be seen in Figure S2, and evidences the particles growth compared to the IrO_x catalyst.

An overview on the distribution of the Ir, Sn, and the doping elements in the IrO_x and IrO_2 materials deposited on the different supports is presented in Figures 2, S7 and S8. Despite some agglomeration, the $\text{IrO}_x/\text{IrO}_2$ nanoparticles are well distributed along the supports. Regarding the Sb, F, and In distributions along the SnO_2 phases in the IrO_x/ATO , IrO_x/FTO , and IrO_x/ITO (Figure S7) catalysts, one can see that the dopants are finely dispersed, and that this dispersion is sustained after the heat treatment at 600 °C for obtaining the rutile IrO_2 -containing materials (Figure S8).

The catalysts' surface compositions were analyzed using the XPS technique. The XPS spectra corresponding to the Ir 4f orbital of the IrO_x catalysts deposited on the different supports are displayed in Figure S9. The spectra can be deconvoluted in two components with Ir 4f_{7/2} peaks centered at 61.8 and 62.5 eV, which correspond to the Ir^{4+} and Ir^{3+} , respectively, and

three shake-up satellites.^[16] The atomic ratio between the Ir^{4+} and Ir^{3+} ($\text{Ir}^{4+}/\text{Ir}^{3+}$) calculated from the XPS data is close to 2/1 for the unsupported and supported IrO_x catalysts.

The high-resolution spectra of the Sn 3d orbital of the IrO_x catalyst supported on SnO_2 , ATO, FTO, and ITO are shown in Figure S10. Here, due to their similar binding energies, the SnO (Sn^{2+}) and SnO_2 (Sn^{4+}) chemical states were not distinguished.^[17] Nonetheless, the Sn 3d spectra can be deconvoluted in two constituents, corresponding to the Sn^0 (3%) and oxidized Sn^{x+} (97%) states.

The XPS spectra of the Sb 3d, F 1s, and In 3d orbitals, i.e. the doping elements in the IrO_x/ATO , IrO_x/FTO , and IrO_x/ITO catalysts, are shown in Figure S11. The Sb 3d spectrum (Figure S11a) can be deconvoluted in two components with Sb 3d_{5/2} peaks centered at 530.1 and 530.9 eV, which correspond to the Sb^{3+} and Sb^{5+} chemical states, respectively.^[18] The F 1s peak at 685.4 eV is assigned to a metal fluoride (M–F) chemical state,^[19] while the In 3d_{5/2} peak at 444.9 eV corresponds to In^{3+} .^[20]

Considering the rutile IrO_2 catalysts obtained after the calcination procedure, the Ir 4f XPS spectra (Figure S12) evidences the conversion of the Ir^{3+} species into Ir^{4+} . In terms of the support materials, no changes are observed comparing the Sn 3d spectra of the hydrous IrO_x (Figure S10) and rutile IrO_2 (Figure S13) containing catalysts, reflecting the thermal stability of the SnO_2 -based supports. However, while Sb and In signals are still present in the IrO_2/ATO and IrO_2/ITO catalysts, no fluorine could be detected in the thin surface layer of IrO_2/FTO material, as shown in Figure S14. This may indicate that fluorine

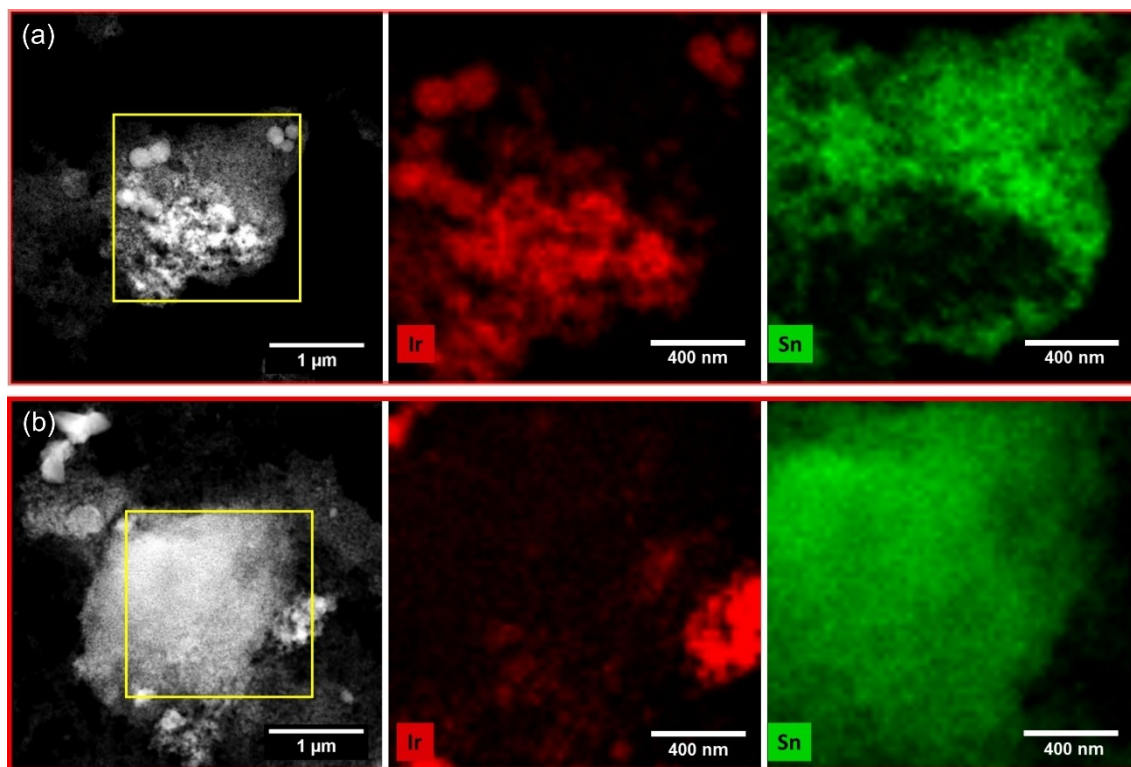


Figure 2. EDX chemical mapping obtained for the a) $\text{IrO}_x/\text{SnO}_2$ and b) $\text{IrO}_2/\text{SnO}_2$ catalysts.

present on the surface of the catalyst is not stable under the calcination procedure.

The electrical conductivities of the Sn-based supports are shown in Table S4. As expected, there is an increase in the electrical conductivity of the doped supports compared to that of pure SnO₂ (5.9E−03 S cm^{−1}), reaching a 20-fold increase for the ATO support (1.1E−01 S cm^{−1}). After the deposition of the IrO_x nanoparticles, an additional increase in conductivity can be observed for the synthesized catalysts, and this is more significant for the IrO_x/SnO₂ (7.0E−02 S cm^{−1}), whose conductivity is comparable to that of IrO_x/ITO material (8.0E−02 S cm^{−1}). Further increase in electrical conductivity is obtained with the conversion of hydrous IrO_x to rutile IrO₂. However, both classes of supported catalyst have lower conductivity compared to that of unsupported IrO_x and IrO₂.

2.2. OER Activity and Stability

The catalysts were initially characterized using experiments of cyclic voltammetry (CV), and the results are exhibited in Figures S15–S16. The CV profile of the unsupported IrO_x material in Figure S15a denotes a pseudocapacitive behavior of the electrode, with a reversible peak at ~0.85 V corresponding to the Ir(III)/Ir(IV) redox couple.^[21] Regarding the IrO_x material deposited on the Sn-based supports, a reduction in the CV currents is seen compared to that of unsupported IrO_x. After the calcination at 600 °C, a capacitive profile is obtained for both unsupported IrO₂ and the supported catalysts, and for these samples, no significant differences are seen in terms of voltammetric charges.

The OER activities of the studied catalysts are displayed in Figure 3. No improvement is observed in the activity of the IrO_x catalysts deposited on the doped-SnO₂ supports, i.e. IrO_x/ATO, IrO_x/FTO, and IrO_x/ITO, in comparison to that of IrO_x/SnO₂ material. For these catalysts, the OER current at 1.55 V is ~3.1 mA cm^{−2}, which is nearly half of the current density obtained for the unsupported catalyst. In terms of mass activity at the same electrode potential, the supported catalysts exhibit a current density of ~41.3 mA mg_{Ir}^{−1}, while for the IrO_x material the mass activity is 85.7 mA mg_{Ir}^{−1}.

Regarding the calcined catalysts, a similar trend can be seen (Figure 3b). The supported catalysts exhibit alike activities, regardless of the presence of dopants, with a current density of ~0.20 mA cm^{−2}, and a mass activity of ~2.7 mA mg_{Ir}^{−1}, both at 1.60 V. For the unsupported IrO₂ material, a current density of 0.36 mA cm^{−2} is obtained, while the mass activity corresponds to 4.9 mA mg_{Ir}^{−1}, which is 1.8-fold higher compared to its supported peers.

The stability of the catalysts was evaluated under a 1,000 cycles aging protocol, and the results are shown in the insets in Figures 3a and 3b. For the unsupported IrO_x catalysts the average OER current decreased from 6.4 mA cm^{−2} to 4.6 mA cm^{−2}, representing a drop of approximately 30%. This confirms the large drop in the OER currents for the IrO_x containing catalysts (Figure 3a, inset), and this is proportionally more pronounced for the supported materials, whose activity

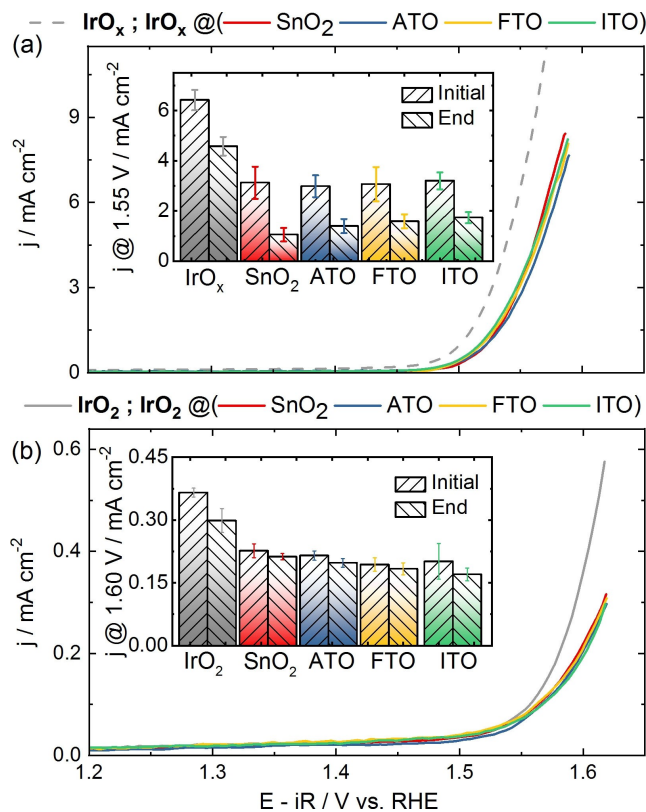


Figure 3. IR-corrected OER polarization curves of the a) IrO_x and b) IrO₂ containing catalysts. The curves were obtained at a sweep rate of 5 mV s^{−1}, in 0.1 M H₂SO₄. Insets: decrease in OER activities of the doped SnO₂-supported IrO_x and IrO₂ materials, at 1.55 V and 1.60 V, respectively, after 1,000 potential cycles between 1.1–1.6 V at 400 mV s^{−1}. Results are the average of three independent measurements.

decreased by ~50% for the IrO_x/ATO, IrO_x/FTO, and IrO_x/ITO catalysts, and by ~65% for the IrO_x/SnO₂ material. A higher stability is obtained after the calcination procedure (Figure 3b, inset), in which the current for the OER decreases by ~10% for the supported catalysts, and by 20% for the unsupported rutile IrO₂.

2.3. Electrochemical Dissolution Stability

The stability of the catalysts in terms of electrochemical dissolution was evaluated using a SFC-ICP-MS setup.^[13] Initially, the elements dissolution was tested during three potential cycles between 1.1–1.6 V and the results are shown in Figures 4, S17 and S18. For all catalysts elements, a first dissolution process, referred to the catalyst contact with the electrolyte under open circuit potential (OCP) conditions, can be observed. Some dissolution is also detected during the ten cleaning cycles between 0.05–1.2 V, and this is especially high for antimony in the IrO_x/ATO material (Figure S17b), which seems to destabilize the IrO_x in the catalyst, resulting in an Ir dissolution signal in the order of 2.2 μg L^{−1}, which is higher compared to the other IrO_x containing catalysts.

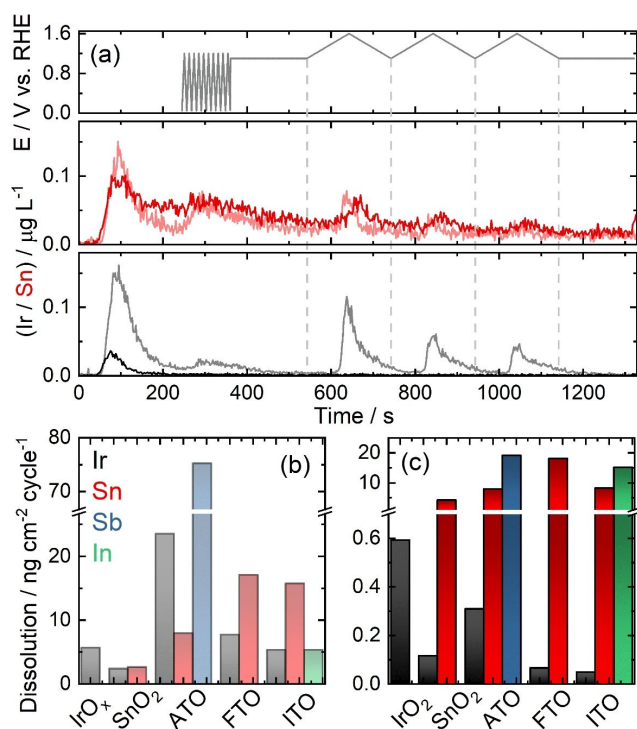


Figure 4. a) IrO_x/SnO₂ and IrO₂/SnO₂ dissolution profiles during three potential cycles between 1.1–1.6 V, at 5 mV s⁻¹, in 0.1 M H₂SO₄. Integrated dissolved amounts of the b) IrO_x and c) IrO₂ containing catalysts during the three cycles.

Regarding the SnO₂-supported IrO_x catalysts, the appearance of Ir, Sn, Sb, and In dissolution peaks is noted during the positive sweep of the multicycles between 1.1–1.6 V, as shown in Figures 4 and S17. Considering the first cycle, the potential onset for Ir dissolution (signal-to-noise S/N=3) is ~1.40 V. The peak intensity for the IrO_x/FTO, IrO_x/ITO, and unsupported IrO_x materials are close to 0.25 $\mu\text{g L}^{-1}$. Lower dissolution is observed for the IrO_x/SnO₂ catalyst (0.10 $\mu\text{g L}^{-1}$), while the iridium phase is less stable in this potential range for the ATO supported material, resulting in a peak intensity of 0.65 $\mu\text{g L}^{-1}$. In the second and third cycles, the Ir dissolution decreases, possibly due to some blockage of active catalyst surface by evolved O₂ bubbles.^[22]

Considering the supports, the onset potentials for Sn, Sb and In dissolutions are, approximately, 1.35 V. Higher dissolution rates are observed for Sn in the IrO_x/FTO and IrO_x/ITO materials (peak intensity of 0.60 $\mu\text{g L}^{-1}$), while considering the Sb and In dopants, a higher peak intensity is seen for the former. Again, for all the support elements, a decrease in dissolution is observed in the second and third cycles. Nonetheless, since Sn, Sb and In signals do not reach 0 $\mu\text{g L}^{-1}$ at the end of the three cycles, constant dissolution when the potential is held at 1.1 V cannot be discarded.

With respect to the calcined materials (Figure 4 and S18), the onset potential for Ir dissolution is ~1.50 V, while a major reduction in the Ir dissolution signals can be observed in comparison to those of the uncalcined IrO_x materials. In terms of supports elements, no change in the onset potentials for Sn,

Sb and In dissolutions is seen, which remains at ~1.35 V. Nonetheless, one can note an important reduction in antimony dissolution (Figure S18b) for the IrO₂/ATO catalyst.

The dissolved amounts during the three cycles between 1.1–1.6 V can be obtained by integration of the dissolution profiles, and the results are shown in Figures 4b and 4c. Considering the hydrous IrO_x catalysts, the Ir dissolution increases in the order SnO₂ < ITO ≈ unsupported < FTO < ATO, ranging from 2.4 to 23.5 $\text{ng cm}^{-2} \text{ cycle}^{-1}$. In terms of Sn dissolution, the catalysts containing the doped supports are less stable compared to IrO_x/SnO₂, with the Sn dissolution increasing in the order SnO₂ < ATO < ITO ≈ FTO, with values ranging from 2.7 to 17.1 $\text{ng cm}^{-2} \text{ cycle}^{-1}$. Regarding the dopants, the Sb and In dissolved amounts are 75.3 and 5.4 $\text{ng cm}^{-2} \text{ cycle}^{-1}$, respectively. The supported rutile catalysts are less prone to Ir dissolution, whose extent follows the order ITO ≈ FTO ≈ SnO₂ < unsupported < ATO, ranging from 0.05 to 0.59 $\text{ng cm}^{-2} \text{ cycle}^{-1}$. In the case of Sn dissolution, the catalysts containing the doped supports are still less stable than the IrO₂/SnO₂ material. However, compared to the IrO_x/SnO₂ (2.7 $\text{ng cm}^{-2} \text{ cycle}^{-1}$), one can note higher Sn dissolution for IrO₂/SnO₂ (4.2 $\text{ng cm}^{-2} \text{ cycle}^{-1}$). Opposite trend is observed for the IrO₂/ITO catalyst (8.0 $\text{ng cm}^{-2} \text{ cycle}^{-1}$), which presents lower Sn dissolution compared to the ITO-supported IrO_x material (15.8 $\text{ng cm}^{-2} \text{ cycle}^{-1}$). For the dopants, one can note a reduction in Sb dissolution (19.1 $\text{ng cm}^{-2} \text{ cycle}^{-1}$), while In dissolution increased (15.1 $\text{ng cm}^{-2} \text{ cycle}^{-1}$) compared to the uncalcined IrO_x/ATO and IrO_x/ITO materials, respectively.

Figure 5 exhibits the dissolution profiles of the SnO₂-supported IrO_x and IrO₂ catalysts during a potential ramp to a final current density of 5 mA cm⁻², while data for the other catalysts can be seen in Figures S19 and S20. Dissolution results make clear the coincidence between the OER and Ir dissolution for the different materials, and the greater stability of Ir in the IrO₂-containing catalysts. The dissolved amounts during this protocol are presented in Figures 5c and 5d. Among the studied hydrous IrO_x catalysts a higher stability is observed for the IrO_x/SnO₂ material, while an increase in Ir and Sn dissolution occurs for catalysts supported on ATO, FTO and ITO. In terms of the dopants, similar to what was presented in Figure 4, Sb dissolution, particularly for the uncalcined IrO_x/ATO catalyst, appears as a major problem.

Finally, the catalysts' dissolution was evaluated using the same protocol employed in the stability studies in the RDE setup, i.e. 1,000 cycles between 1.1–1.6 V at 400 mV s⁻¹. The results for the IrO_x/SnO₂ and IrO₂/SnO₂ catalysts are presented in Figure 6, while data for the other materials can be seen in Figures S21 and S22. In the case of iridium in IrO_x containing catalysts, the dissolution rate decreases throughout the aging protocol (Figure 6a and S21), which is a behavior similar to that of the IrO₂ catalysts (Figure S22a). Higher Ir dissolution is observed by considering the results for the initial three cycles between 1.1–1.6 at 5 mV s⁻¹, and those for the three cycles recorded after the aging procedure. Considering the supports, similar trends are observed for the dissolution of Sn, Sb, and In.

The calculated dissolved amounts of the studied catalysts are exhibited in Figures 6b and 6c. Similar to what was obtained

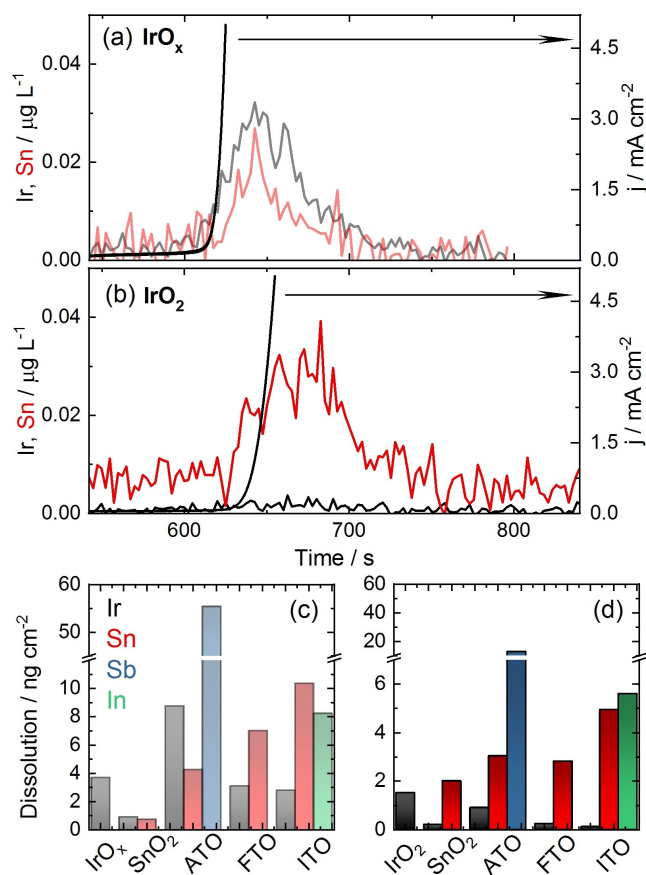


Figure 5. a) $\text{IrO}_x/\text{SnO}_2$ and b) $\text{IrO}_2/\text{SnO}_2$ dissolution profiles during a potential ramp to a current density of 5 mA cm^{-2} , in $0.1 \text{ M H}_2\text{SO}_4$. Integrated dissolved amounts of the c) IrO_x and d) IrO_2 containing catalysts.

in the three cycles (Figure 4) and in the ramp (Figure 5) testing protocols, lower iridium dissolution is obtained for the $\text{IrO}_x/\text{SnO}_2$, IrO_x/FTO and IrO_x/ITO catalysts compared to the unsupported IrO_x material, while higher dissolution is detected for the IrO_x/ATO catalyst. Regarding the support, the $\text{IrO}_x/\text{SnO}_2$ material shows higher stability in terms of Sn dissolution compared to the ATO-, FTO-, and ITO-supported IrO_x catalysts. For the calcined catalysts, a decrease in Ir dissolution is observed for the supported samples compared to that of IrO_2 . Also higher Sn dissolution is detected for the catalysts containing the doped- SnO_2 supports. In the case of the IrO_x/ATO and IrO_2/ATO catalysts along the 1,000 aging cycles, it is noted that Sb dissolution is lower for the calcined sample. On the other hand, the Sn dissolution in this material increases compared to that of the IrO_x/ATO catalyst.

3. Discussion

3.1. Physicochemical and Electrochemical Characterization of Catalysts

In order to investigate the feasibility of doped- SnO_2 as supports for oxygen evolution reaction (OER), SnO_2 -, ATO-, FTO-, and ITO-

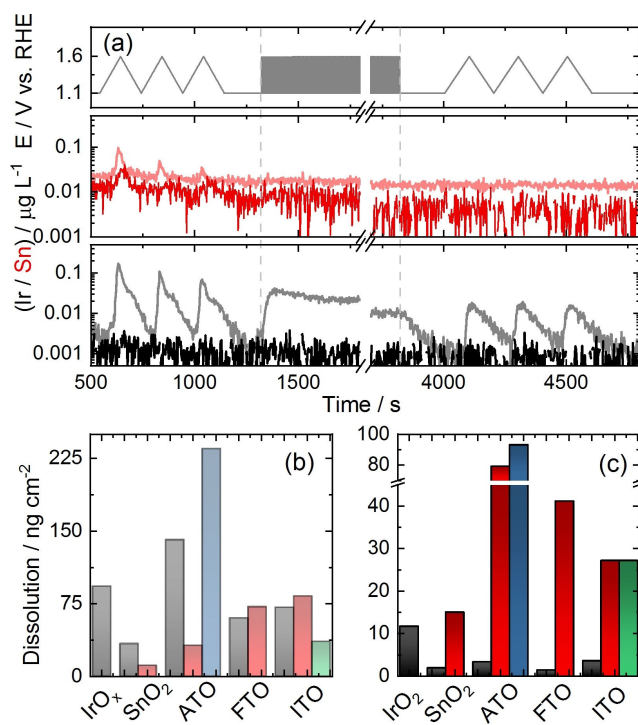


Figure 6. a) $\text{IrO}_x/\text{SnO}_2$ and $\text{IrO}_2/\text{SnO}_2$ dissolution profiles during 1,000 potential cycles between 1.1–1.6 V, at 400 mV s^{-1} , in $0.1 \text{ M H}_2\text{SO}_4$. Integrated dissolved amounts of the b) IrO_x and c) IrO_2 containing catalysts.

supported hydrous IrO_x and rutile IrO_2 electrocatalysts were synthesized and characterized. The amorphous nature of IrO_x is confirmed by the XRD data (Figure 1a and S1a), in which only the diffraction peaks relative to the SnO_2 structure is observed. In fact, the IrO_x phase is a hydrated oxyhydroxide, which can be converted to rutile IrO_2 by heating,^[10] as confirmed by the XRD data in Figures 1a and S1b. Further insight into the conversion of IrO_x to IrO_2 is obtained by XPS analyses (Figures S9 and S12), which show the existence of Ir^{3+} oxidation state for the IrO_x containing materials, and the conversion to Ir^{4+} in the calcined samples.

The TEM micrographs and EDX chemical maps confirm that the $\text{IrO}_x/\text{IrO}_2$ nanoparticles are well distributed along the supports. Similar results are obtained considering the dopants (Sb, F, and In) dispersion; no segregation occurs with further calcination for obtaining the IrO_2 containing catalysts. However, while Sb and In are still detected on the IrO_2/ATO and IrO_2/ITO catalysts surface, as shown in the XPS results in Figure S14, for the IrO_2/FTO catalyst, no signal corresponding to F 1s orbital was detected (Figure S14b), which may imply in degradation of the doped FTO support during the heat treatment.

Considering the electrical conductivity of the synthesized supports, a 3.4-, 8.3-, and 18.6-fold increase is attained for the ITO, FTO, and ATO materials, respectively, compared to the undoped SnO_2 support. Nonetheless, the electrical conductivity of the SnO_2 -based supports reported in Table S4 is still lower as compared to that reported for carbon Vulcan (21.6 S cm^{-1}),^[6b] which is usually employed as support for many electrocatalysts. After the deposition of the IrO_x nanoparticles, the electrical

conductivity of the catalysts increased compared to that of the supports. Karimi and Peppley also reported a similar trend for oxides (ATO and NbO₂) and carbide supported (TiC) iridium nanoparticles.^[23] Further increase in electrical conductivity is obtained after the heat treatment of the catalysts, which can be attributed to the conversion of the IrO_x nanoparticle to IrO₂, as evidenced by the conductivity data of the pristine materials.

Results of cyclic voltammetry evidence a reduction in the voltammetric charge of the supported IrO_x catalysts compared to that of the pristine IrO_x material, which can be assigned to the lower electrical conductivity caused by the presence of the SnO₂-based supports (Figure S15). On the other hand, for the calcined samples these differences are minimized, resulting in similar capacitive charges for all IrO₂ containing catalysts (Figure S16).

3.2. OER Activity and Stability of Catalysts

De Pauli and Trasatti showed that the activity of SnO₂+IrO₂ catalysts increased dramatically when the amount of Ir increased up to about 20 mol% IrO₂, and remained nearly constant for higher iridium loadings, which is assigned to the saturation of the support particle surface by IrO₂.^[24] Tong et al. also reported poorer OER activity for ATO supported IrO₂ catalysts, with IrO₂ loading up to 31%, in comparison to pure IrO₂. For a catalyst with 50% of IrO₂, however, the performance surpassed that of IrO₂.^[25] On the other hand, higher catalytic activities for mixed and supported catalyst, even with lower iridium loadings have been described.^[26] Here, the OER polarization curves in Figure 3a evidence that the supported IrO_x catalysts are less active compared to unsupported IrO_x. All these results suggest that a thorough investigation into the effect of Ir loading on the catalytic performance of the supported catalysts is still required.

Considering the supported IrO_x materials, no significant difference is observed in the polarization curves of the ATO-, FTO-, and ITO-supported catalysts and that of the IrO_x/SnO₂ material, which is most likely related to the gain in electrical conductivity caused by the deposition of the IrO_x nanoparticles on the SnO₂ (Table S4). Similar results were shown recently for IrO_x supported on SnO₂, Sb-SnO₂, and Ta-SnO₂ catalysts.^[27]

The IrO₂ containing catalysts (Figure 3b) exhibit lower OER activity compared to their IrO_x peers. The better performance of hydrous IrO_x is still under debate, but it is usually explained based on the presence of Ir³⁺ and Ir-OH species,^[28] in addition to vacancies in the oxygen electronic structure,^[28a] and the existence of an electrophilic O¹⁻ specie, which reduces the activation energy for H₂O adsorption.^[29] For these catalysts, similarly to the IrO_x containing materials, the pristine IrO₂ is more active compared to the supported catalysts, and also no gain in performance is obtained using the doped or undoped SnO₂ supports.

In terms of stability, a larger drop in performance is seen for the hydrous IrO_x catalysts, while the IrO₂ materials, in particular the supported catalysts, are more stable. These results are in

line with previous studies on the stability of hydrous and rutile iridium oxide.^[30]

3.3. Dissolution of Catalysts

The electrochemical dissolution of the studied materials was investigated in order to evaluate the feasibility of using Sb-, F-, and In-doped SnO₂ as supports for OER electrocatalysts. A release of the supports components to the solution under OCP conditions (Figures 4, S17, S18) is observed, and this can be explained by the chemical dissolution of the oxides, as proposed by Geiger et al. in the study of ATO, FTO, and indium tin oxide films.^[9] While cycled between 1.1–1.6 V, one can note the increase in Sn, Sb, and In dissolutions during the positive sweep, which indicates the occurrence of an electrochemical, instead of a chemical process, as already observed during the anodic polarization in a broader potential range.^[9] Nonetheless, during the second and third cycles, the dissolution of the supports constituents decrease, indicating some stabilization of the materials.

The dissolved amounts of elements in Figures 4b and 4c, clearly denote that the Sn release is enhanced for the catalysts containing the doped supports in comparison to that of SnO₂-supported IrO_x and IrO₂ materials. Besides, the dopants dissolution cannot be ignored. The calculated Sb and In mass release for the IrO_x/ATO (75.3 ng cm⁻² cycle⁻¹) and IrO_x/ITO (5.4 ng cm⁻² cycle⁻¹) catalysts represents a loss of ~0.28% and ~0.03% in relation to the initial contents. For the calcined samples, the Sb and In dissolutions represents a mass reduction of ~0.07% and 0.09%, respectively, in each cycle. Recently, tin and antimony dissolution was also observed during the ex situ ICP-MS analysis of the exhaust water from the anode of a PEMWE,^[31] revealing instability of these elements in the polymer electrolyte environment too.

In the case of iridium, the higher dissolution rates for the IrO_x catalysts compared to their IrO₂ peers are in line with previous works sustaining that, while the hydrous oxide is more active for the OER, greater stability is demonstrated by the crystalline material.^[30b,32] The dissolved amounts in Figure 3b suggest that some enhancement of Ir stability can be gained by supporting IrO_x on SnO₂, while the lower stability of the ATO support causes an opposite effect, which indicates that here the electrocatalyst-support interaction does not help catalyst stabilization, as observed previously for Ir/IrO_x/ATO.^[33] In contrast, all supported crystalline IrO₂ materials exhibit Ir dissolution lower than the pristine material.

It has been observed that the OER and iridium dissolution share common intermediates,^[34] therefore polarizing the catalysts at the same current density provides a fairer analysis of iridium dissolution. The dissolution results obtained during a ramp to final current density of 5 mA cm⁻² (Figures 5, S19, and S20) confirm the stabilizing role of the SnO₂ support for the IrO_x nanoparticles, as well as the lower Sn loss in comparison to the doped supports.

A useful metric to compare the stability of the studied catalysts is the so-called stability number (S-number).^[35] The S-

number is defined as the ratio of the number of moles of formed O_2 and of dissolved Ir, that does not depend on the iridium loading, the surface area, or the nature of the active sites involved in the OER. The higher the S-number, the greater is the stability of the catalyst. The calculated S-number for the IrO_x/SnO_2 catalyst is $1.6E+04$, representing nearly a 3-fold increase compared to IrO_x ($5.8E+03$). On the other hand, the S-number for the IrO_x/ATO catalyst is $2.5E+03$, confirming its lower stability. Considering the calcined catalysts, the S-number for the IrO_2 material is $1.5E+04$, which is lower than that for SnO_2 - ($1.2E+05$), ATO- ($5.3E+04$), FTO- ($1.8E+05$), and ITO-supported ($2.6E+05$) IrO_2 catalysts.

Dissolution was also monitored during a longer stability test protocol, comprising 1,000 potential cycles between 1.1–1.6 V, similar to the study in the RDE setup. The data presented in Figures S6, S21, and S22 show that the elements dissolution decreases along the aging protocol. For the IrO_x -containing catalyst, the decrease in the Ir release can be attributed, to a small extent, to some conversion of IrO_x to IrO_2 along the aging test.^[36] However, blockage by O_2 bubbles may be the main cause of this decline.^[22] The dissolved amount of Ir for the pristine IrO_x material (93 ng cm^{-2}) during the whole accelerated aging protocol corresponds to about 0.10% of the initial mass. Although relatively small, this Ir loss may contribute to the reduction of lifetime of PEMWE during long time operations. Besides, dissolution is considered a primary degradation phenomenon, which may trigger secondary degradation mechanisms^[37] like particles growth and coalescence.^[30a,38]

Considering the supported IrO_x catalysts, in a similar way to the previous cases, higher Ir stability is observed for the IrO_x/SnO_2 catalyst (34 ng cm^{-2}), while IrO_x/ATO exhibits large Ir dissolution during the test, close to 140 ng cm^{-2} , corresponding to a mass loss of $\sim 0.14\%$. The FTO- and ITO-supported IrO_x catalysts also shows lower Ir dissolution compared to unsupported IrO_x . Nonetheless, the support degradation is confirmed as a problem, since Sn dissolution increases in the order $SnO_2 < ATO < FTO < ITO$. Considering Sb and In, the loss corresponds to 0.88% and 0.22% of the initial mass of the dopants, respectively, which also may become a major problem during longer tests under real PEMWE operations.

Since the doped- SnO_2 supported IrO_x/IrO_2 catalysts are not more active or stable compared to the materials supported on SnO_2 , a conclusion can be drawn that the use of dopants in tin oxides is not the best solution for producing superior catalysts. However, some clarification is required. First, depending on the synthesis method, strong metal-support interaction (SMSI) may occur,^[33] although it is still to be proven if SMSI is indeed beneficial for activity or stability of tin oxides. Second, other dopants, like tantalum, which show higher stability,^[27] must be further explored. Finally, the conclusions drawn for the performance of catalysts or supports in aqueous RDE and SFC environment may not be always extrapolated to real PEMWE.^[27,35] In particular, concerning the difference in conductivity, for thicker catalyst layers significant potential losses are expected. Although, since iridium oxide is a good electronic conductor, such losses may be tolerable. These aspects are still to be clarified.

4. Conclusions

In this work, the OER activity and stability of ATO-, FTO-, and ITO-supported IrO_x and IrO_2 catalysts were investigated, combining both rotating disk electrode (RDE) and a scanning flow cell hyphenated to an inductively coupled plasma mass spectrometer (SFC-ICP-MS) setups. It is shown that the IrO_x/SnO_2 and IrO_2/SnO_2 materials present activities similar to those of the catalysts prepared using the doped supports, which is attributed to the similar increase in conductivity caused by the deposition of iridium oxide nanoparticles.

The stability of the studied materials was investigated in terms of dissolution under three protocols. Considering the supports, doping the SnO_2 causes an increase in Sn dissolution in comparison to the materials supported on the pristine SnO_2 . Besides, the dopants elements also dissolve, and this is especially critical for Sb, which also seems to destabilize the IrO_x phase, leading to a higher Ir dissolution, also compared to unsupported IrO_x . These results can be even more critical during longer testing and PEMWE applications.

Since no benefits are observed in either activity or stability, the need to use dopants over pure SnO_2 becomes questionable, which suggests that strategies are needed to obtain more stable doped- SnO_2 supports.

Acknowledgements

The authors thank Dr. Marcelo Calegaro for the XRD analysis. G.C.d.S. and E.A.T. thank the financial support from FAPESP (n 2013/16930-7). G.C. d.S. thanks CNPq for the sandwich PhD scholarship (n 200321/2017-0). S.C. thanks the DFG for financial support within the grant CH 1763/4-1 and funding by the German Federal Ministry of Education and Research (BMBF) within the Kopernikus Project P2X.

Conflict of Interest

The authors declare no conflict of interest.

Keywords: oxygen evolution · iridium oxide · tin oxide · dopants · dissolution

- [1] a) J. O. Abe, A. P. I. Popoola, E. Ajenifuja, O. M. Popoola, *Int. J. Hydrogen Energy* **2019**, *44*, 15072–15086; b) N. Armadori, V. Balzani, *ChemSusChem* **2011**, *4*, 21–36; c) A. S. Aricò, S. Siracusanò, N. Briguglio, V. Baglio, A. Di Blasi, V. Antonucci, *J. Appl. Electrochem.* **2013**, *43*, 107–118.
- [2] M. Busch, *Curr. Opin. Electrochem.* **2018**, *9*, 278–284.
- [3] C. Wang, F. Lan, Z. He, X. Xie, Y. Zhao, H. Hou, L. Guo, V. Murugadoss, H. Liu, Q. Shao, *ChemSusChem* **2019**, *12*, 1576–1590.
- [4] E. Fabbri, A. Habereder, K. Waltar, R. Kötz, T. J. Schmidt, *Catal. Sci. Technol.* **2014**, *4*, 3800–3821.
- [5] E. Antolini, *Appl. Catal. B* **2009**, *88*, 1–24.
- [6] a) C. Spöri, J. T. H. Kwan, A. Bonakdarpour, D. P. Wilkinson, P. Strasser, *Angew. Chem. Int. Ed.* **2017**, *56*, 5994–6021; *Angew. Chem.* **2017**, *129*, 6088–6117; b) T. Reier, H. N. Nong, D. Teschner, R. Schlögl, P. Strasser, *Adv. Energy Mater.* **2017**, *7*, 1601275.
- [7] H. S. Oh, H. N. Nong, P. Strasser, *Adv. Funct. Mater.* **2015**, *25*, 1074–1081.

- [8] a) H. S. Oh, H. N. Nong, T. Reier, M. Gliech, P. Strasser, *Chem. Sci.* **2015**, *6*, 3321–3328; b) V. K. Puthiyapura, M. Mamlouk, S. Pasupathi, B. G. Pollet, K. Scott, *J. Power Sources* **2014**, *269*, 451–460; c) V. K. Puthiyapura, S. Pasupathi, H. Su, X. Liu, B. Pollet, K. Scott, *Int. J. Hydrogen Energy*, **2014**, *39*, 1905–1913; d) H. Ohno, S. Nohara, K. Kakinuma, M. Uchida, H. Uchida, *Catalysts*, **2018**, *9*, 74–85; e) B. Han, M. Risch, S. Belden, S. Lee, D. Bayer, E. Mutoro, Y. Shao-Horn, *J. Electrochem. Soc.* **2018**, *165*, F813–F820.
- [9] S. Geiger, O. Kasian, A. M. Mingers, K. J. J. Mayrhofer, S. Cherevko, *Sci. Rep.* **2017**, *7*, 4595.
- [10] N. Bestaoui, E. Prouzet, *Chem. Mater.* **1997**, *9*, 1036–1041.
- [11] H. Rietveld, *J. Appl. Crystallogr.* **1969**, *2*, 65–71.
- [12] S. Zhang, C. Scheu, *Microscopy* **2018**, *67*, i133–i141.
- [13] O. Kasian, S. Geiger, K. J. J. Mayrhofer, S. Cherevko, *Chem. Rec.* **2018**, *19*, 2130–2142.
- [14] E. V. Sokovykh, L. P. Oleksenko, N. P. Maksymovych, I. P. Matushko, *J. Therm. Anal. Calorim.* **2015**, *121*, 1159–1165.
- [15] C. Felix, T. Maiyalagan, S. Pasupathi, B. Bladergroen, V. Linkov, *Micro Nanosyst.* **2012**, *4*, 186–191.
- [16] V. Pfeifer, T. E. Jones, J. J. Velasco Vélez, C. Massué, M. T. Greiner, R. Arrigo, D. Teschner, F. Girgsdies, M. Scherzer, J. Allan, M. Hashagen, G. Weinberg, S. Piccinin, M. Hävecker, A. Knop-Gericke, R. Schlögl, *Phys. Chem. Chem. Phys.* **2016**, *18*, 2292–2296.
- [17] a) D. Briggs, *Surf. Interface Anal.* **1981**, *3*, v–v; b) P. Stefanov, G. Atanasova, E. Manolov, Z. Raicheva, V. Lazarova, *J. Phys. Conf. Ser.* **2008**, *100*, 082046.
- [18] Y. Li, J. Sun, W. Mao, S. Tang, K. Liu, T. Qi, H. Deng, W. Shen, L. Chen, L. Peng, *Microchim. Acta* **2019**, *186*, 403.
- [19] W. Z. Samad, M. M. Salleh, A. Shafiee, M. A. Yarmo, *Sains Malays.* **2011**, *40*, 251–257.
- [20] K. Siuzdak, M. Szkoda, J. Karczewski, J. Ryl, K. Darowicki, K. Grochowska, *Acta Metall. Sin. (Engl. Lett.)* **2017**, *30*, 1210–1220.
- [21] a) S. Gottesfeld, S. Srinivasan, *J. Electroanal. Chem. Interfacial Electrochem.* **1978**, *86*, 89–104; b) L. Ouattara, S. Fierro, O. Frey, M. Koudelka, C. Cominellis, *J. Appl. Electrochem.* **2009**, *39*, 1361–1367.
- [22] H. A. El-Sayed, A. Weiß, L. F. Olbrich, G. P. Putro, H. A. Gasteiger, *J. Electrochem. Soc.* **2019**, *166*, F458–F464.
- [23] F. Karimi, B. A. Peppley, *Electrochim. Acta.* **2017**, *246*, 654–670.
- [24] C. P. De Pauli, S. Trasatti, *J. Electroanal. Chem.* **2002**, *538–539*, 145–151.
- [25] J. Tong, Y. Liu, Q. Peng, W. Hu, Q. Wu, *J. Mater. Sci.* **2017**, *52*.
- [26] a) C. Massué, V. Pfeifer, X. Huang, J. Noack, A. Tarasov, S. Cap, R. Schlögl, *ChemSusChem* **2017**, *10*, 1943–1957; b) E. Balko, P. Nguyen, *J. Appl. Electrochem.* **1991**, *21*, 678–682.
- [27] L. Solà-Hernández, F. Claudel, F. Maillard, C. Beauger, *Int. J. Hydrogen Energy* **2019**, *44*, 24331–24341.
- [28] a) V. Pfeifer, T. E. Jones, J. J. Velasco Vélez, C. Massué, R. Arrigo, D. Teschner, F. Girgsdies, M. Scherzer, M. T. Greiner, J. Allan, *Surf. Interface Anal.* **2016**, *48*, 261–273; b) D. F. Abbott, D. Lebedev, K. Waltar, M. Povia, M. Nachtegaal, E. Fabbri, C. Copéret, T. J. Schmidt, *Chem. Mater.* **2016**, *28*, 6591–6604.
- [29] a) V. Pfeifer, T. E. Jones, J. J. Velasco Vélez, R. Arrigo, S. Piccinin, M. Hävecker, A. Knop-Gericke, R. Schlögl, *Chem. Sci.* **2017**, *8*, 2143–2149; b) V. A. Saveleva, L. Wang, D. Teschner, T. Jones, A. S. Gago, K. A. Friedrich, S. Zafeiratos, R. Schlögl, E. R. Savinova, *J. Phys. Chem. Lett.* **2018**, *9*, 3154–3160.
- [30] a) G. C. da Silva, N. Perini, E. A. Ticianelli, *Appl. Catal., B* **2017**, *218*, 287–297; b) S. Cherevko, S. Geiger, O. Kasian, A. Mingers, K. J. J. Mayrhofer, *J. Electroanal. Chem.* **2016**, *774*, 102–110.
- [31] I. Jiménez-Morales, S. Cavaliere, M. Dupont, D. Jones, J. Rozière, *Sustainable Energy Fuels* **2019**, *3*, 1526–1535.
- [32] P. Jovanovič, N. Hodnik, F. Ruiz-Zepeda, I. Arčon, B. Jozinovič, M. Zorko, M. Bele, M. Šala, V. S. Šelih, S. Hočevar, *J. Am. Chem. Soc.* **2017**, *139*, 12837–12846.
- [33] H.-S. Oh, H. N. Nong, T. Reier, A. Bergmann, M. Gliech, J. Ferreira de Araújo, E. Willinger, R. Schlögl, D. Teschner, P. Strasser, *J. Am. Chem. Soc.* **2016**, *138*, 12552–12563.
- [34] a) S. Cherevko, S. Geiger, O. Kasian, A. Mingers, K. J. Mayrhofer, *J. Electroanal. Chem.* **2016**, *774*, 102–110; b) S. Cherevko, S. Geiger, O. Kasian, A. Mingers, K. J. Mayrhofer, *J. Electroanal. Chem.* **2016**, *773*, 69–78; c) O. Kasian, J. P. Grote, S. Geiger, S. Cherevko, K. J. Mayrhofer, *Angew. Chem. Int. Ed.* **2018**, *57*, 2488–2491; *Angew. Chem.* **2018**, *130*, 2514–2517.
- [35] S. Geiger, O. Kasian, M. Ledendecker, E. Pizzutilo, A. M. Mingers, W. T. Fu, O. Diaz-Morales, Z. Li, T. Oellers, L. Fruchter, *Nat. Can.* **2018**, *1*, 508.
- [36] T. Li, O. Kasian, S. Cherevko, S. Zhang, S. Geiger, C. Scheu, P. Felfel, D. Raabe, B. Gault, K. J. J. Mayrhofer, *Nat. Can.* **2018**, *1*, 300.
- [37] J. C. Meier, C. Galeano, I. Katsounaros, J. Witte, H. J. Bongard, A. A. Topalov, C. Baldizzone, S. Mezzavilla, F. Schüth, K. J. J. Mayrhofer, *Beilstein J. Nanotechnol.* **2014**, *5*, 44–67.
- [38] F. Claudel, L. Dubau, G. Berthomé, L. Sola-Hernandez, C. Beauger, L. Piccolo, F. Maillard, *ACS Catal.* **2019**, *9*, 4688–4698.

Manuscript received: March 11, 2020

Revised manuscript received: April 17, 2020

Accepted manuscript online: April 24, 2020